Title: Heat dissipation in 3D printed cellular aluminum nitride structures

Corresponding Author: Dr. Manuel Belmonte,

Corresponding Author's Institution: Instituto de Cerámica y Vidrio

First Author: Manuel Belmonte

Order of Authors: Manuel Belmonte; Gonzalo López-Navarrete; Isabel Osendi; Pilar Miranzo

Abstract: The improvement of heat dissipation in electronic and energy devices is a challenge that can be addressed through the use of highly porous materials. Presently, the additive manufacturing of 3D aluminum nitride is described, and different lattices patterns with corresponding porosities in the range 45-64% are achieved by direct ink writing. All the structures are robust and the effective thermal conductivity (keff) for cuboid structures decreases by 50-75% with the filament separation and shows anisotropic characteristics, since keff along the longitudinal axis of the scaffold is up to six times greater than for the transversal. Heat transfer during free cooling experiments for cuboid and cylinder scaffolds, after rapid heating at temperatures above 1000 °C, takes place by radiation for temperatures 500°C and by convection through the complete cooling process. The heat dissipation time constants of both processes decrease almost linearly with the designed scaffold parameters of porosity and rod separation.

Research Data Related to this Submission

There are no linked research data sets for this submission. The following reason is given:
Data will be made available on request

Highlights

- 3D printing allows tailoring the thermal performance of cellular materials

- Mechanically robust 3D cellular AlN architectures are additive manufactured

- The cellular pattern controls the effective thermal conductivity and heat dissipation

- Heat dissipation is governed by convection and radiation

- Heat dissipation increases with the scaffold macroporosity and rod separation

Heat dissipation in 3D printed cellular aluminum nitride structures

Manuel Belmonte[*], Gonzalo Lopez-Navarrete, M. Isabel Osendi, Pilar Miranzo

Institute of Ceramics and Glass (ICV-CSIC), Kelsen 5, 28049 Madrid, Spain

Abstract

The improvement of heat dissipation in electronic and energy devices is a challenge that can be addressed through the use of highly porous materials. Presently, the additive manufacturing of 3D aluminum nitride is described, and different lattices patterns with corresponding porosities in the range 45-64% are achieved by direct ink writing. All the structures are robust and the effective thermal conductivity (k_{eff}) for cuboid structures decreases by 50-75% with the filament separation and shows anisotropic characteristics, since k_{eff} along the longitudinal axis of the scaffold is up to six times greater than for the transversal. Heat transfer during free cooling experiments for cuboid and cylinder scaffolds, after rapid heating at temperatures above 1000 ºC, takes place by radiation for temperatures >500ºC and by convection through the complete cooling process. The heat dissipation time constants of both processes decrease almost linearly with the designed scaffold parameters of porosity and rod separation.

---

[*] Corresponding author. Phone: +34-917355863; Fax: +34-917355843. E-mail: mbelmonte@icv.csic.es (M. Belmonte)

1. Introduction

The constant increases of power density and integration in electronic devices prompt to research in systems with improved thermal dissipation and, thus, to avoid device overheating and loss of functionality. Aluminum nitride (AlN) ceramics are non-toxic materials of high thermal conductivity -320 $W \cdot m^{-1} \cdot K^{-1}$ at room temperature for a single crystal [1]- with a low dielectric constant, and thermal expansion coefficient close to that of silicon [2], which are used as substrates in high-quality electronic packaging [3]. In particular, these ceramics are employed for distinct power modules in all-electric and hybrid-electric vehicles [4]. Besides, dense AlN materials have attracted interest for encapsulating high-temperature silicon carbide converters and in microelectromechanical systems [5]. Until now, dense parts of highly thermal conductive AlN have been developed by tape casting [6], gel casting [7,8] and injection molding [9]. In addition, complex AlN parts could also be used in patterned designed multi-chip modules, such as high-power light-emitting diodes (HP-LEDs) [10], where the thermal dissipation is a key parameter. In this sense, 3D architectures based on porous channels and a high thermal conductive ceramic skeleton would be a promising solution for many engineering and industrial applications linked to thermal managing, mainly due to its light weight and enhanced heat transfer by conduction and convection. Hence, other fabrication technologies are required and, in this sense, additive manufacturing (AM) of 3D highly porous structures stands out as a promising solution. We can only refer to a handful of works devoted to the AM of AlN parts [11-14]. In this way, Jankowski et al. [11] fabricated by stereolithography dense AlN microchannel integrated substrates for cooling semiconductor power devices, aiming at reducing the number of thermally resistive layers in power electronics packages, and reported a thermal conductivity of 165 $W \cdot m^{-1} \cdot K^{-1}$. Recently, Diaz-Moreno et al. [12] used binder

2

jetting and hot isostatic pressing to manufacture porous AlN specimens (~60% of the theoretical density) with a room temperature conductivity of ~5 $W \cdot m^{-1} \cdot K^{-1}$. Conversely, Huang et al. [13] employed fuse deposition modeling for 3D printing AlN materials, although no detailed information on density and thermal properties was provided in the filed patent. Finally, Duan et al. [14] lately reported the digital light processing of AlN dense complex parts (4% of porosity) of high thermal conductivity (155 $W \cdot m^{-1} \cdot K^{-1}$). Therefore, new studies on the thermal performance of additive manufactured AlN parts are necessary to further progress in the development of thermal conductive and heat dissipative AlN structures. Accordingly, the goals of the present work are to AM 3D cellular AlN architectures with distinct shapes (cuboids and cylinders), patterned designs (orthogonal and radial) and macroporosities (different span distances) and, afterwards, to establish their thermal conductivity and heat dissipation characteristics. These architectures are produced for the first time by Robocasting [15,16], a direct ink writing technique that allows building scaffolds in a layer-by-layer sequence from aqueous pseudoplastic inks, generally containing high amount of solids and low percentage of organic additives, thus, enabling subsequent enhancement of the mechanical integrity during the sintering of the ceramic skeleton.

2. Experimental

The AlN ceramic powder composition was prepared by powder mixing 97 wt.% of AlN (Grade C, H.C. Starck GmbH, particle size in the range of 0.8-2.0 μm) and 3 wt.% of Y_2O_3 (Grade C, H.C. Starck GmbH, mean particle size $d_{50} = 0.9$ μm). The Y_2O_3 content was selected because it promotes the densification of AlN and captures oxygen from the ceramic lattice, which, therefore, contributes to increase the thermal conductivity

3

[17,18]. The powder composition was homogenized by ball milling (polytetrafluoroethylene balls) in isopropyl alcohol media for 90 min. Then, alcohol was removed in a rotary evaporator and the powder mix was dried at 120 ºC overnight and, afterwards, sieved through a 63 μm mesh.

Next, a printable AlN ink was developed by mixing the powder composition, ultrapure water, and a set of organics in adequate proportions. The organics helped to get viscoelastic behavior and high storage modulus to the ink. For that purpose, high molecular weight polyethylenimine (H-PEI, PEI 25000, Sigma Aldrich; < 1 wt.% of water content) and low molecular weight PEI (L-PEI, PEI 2000, Sigma Aldrich; 50 wt.% of water content) were added as dispersants, promoting electrostatic and steric repulsions that allowed higher solid contents in the ink formulation. Afterwards, a viscosifier, such as methylcellulose (MC, Methocel F4M, Dow Chemical Co.; 95 wt.% of water content), was added to produce a weak gel and, finally, the process was completed by incorporating polyacrylic acid (PAA, Alfa Aesar, 75 wt.% of water content), an anionic polyelectrolyte, to induce flocculation. All components (ceramic powders, water and organics) were sequentially added and homogenized at 1100 rpm for 30 s in a planetary centrifugal mixer (ARE-250, Thinky Co.) that contained Si_3N_4 milling balls. The rheological behavior of the ink was analyzed at a constant temperature of 25 °C using a rheometer (CVO 100 D, Bohlin Instruments) equipped with a cone-and-plate geometry (diameter: 40 mm; cone angle: 4°). The apparent viscosity (η) versus the shear rate ($\dot{\gamma}$) was measured from 0.05 to 100 s^{-1}; while the shear storage (G') and loss (G'') moduli were recorded as a function of the shear stress (τ) using oscillation amplitude sweep tests at a frequency of 1 Hz and ascending stress sweeps from 0.5 to 1000 Pa.

Various sets of 3D AlN periodic lattices with distinct dimensions and patterns were computer designed (RoboCAD 4.0, 3-D Inks LLC) employing nozzle tips with an inner diameter of 330 μm (Precision Tips; Nordson EFD Inc.). In particular, three types of square cuboids ("S") of 12 x 12 x 6 mm^3 (24 layers with a linear array of parallel filaments in the x-y plane, each array rotated 90° respect the adjacent layers) with different distance between in-plane adjacent rods ("a_{CAD}") were designed in the CAD file (Figure 1a-c), namely: i) S-H for a_{CAD} = 1.22 mm, ii) S-S, a_{CAD} = 0.90 mm and iii) S-L with a_{CAD} = 0.60 mm. Accordingly, structures containing 64, 144 and 324 cells, respectively, were produced. The "H", "S" and "L" lettering corresponds to high, standard, and low distances, respectively. Besides, two cylindrical ("C") periodic lattices (20 layers) of 5.0 mm of height and 14.0 mm of diameter were designed (Figure 1d,e) and labelled as: i) "C-H" for the so-called standard pattern of orthogonal layers, a_{CAD} = 1.22 mm and 86 cells and ii) "C-R" with a radial pattern of 67 cells. All structures were printed in air onto flat alumina substrates with a three-axis robocasting system (A-3200, 3-D Inks LLC), where the X-Y table velocity was set at 10 mm·s^{-1}.
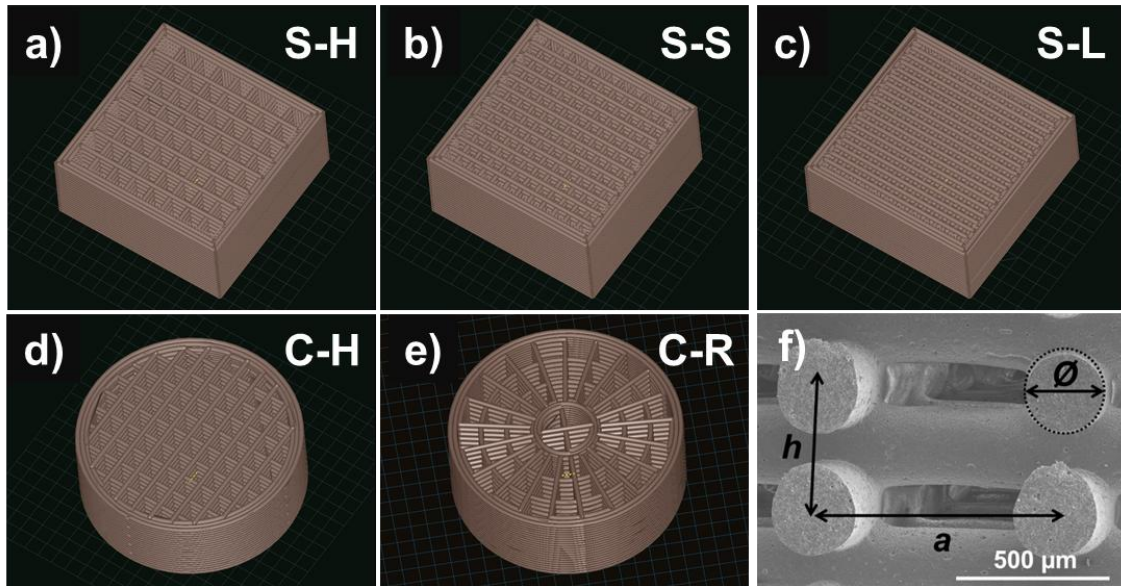
Figure 1. a-e) Computer designed square cuboid (S) and cylindrical (C) periodic lattices with different patterned structure, including variations in the distance between in plane adjacent rods (a-c) for cuboid scaffolds and two types of lattices for the cylindrical ones (d-e). f) FESEM image of a cross-section for a sintered AlN S-S cuboid with main cell parameters overlaid (Ø = mean diameter of the rods, a = distance between two adjacent rods, h = distance between two equivalent layers in the z-direction).

In order to choose a heating schedule for removing the organics employed in the ink formulation, and avoiding at the same time the AlN oxidation , thermogravimetric-differential thermal analysis (TGA-DTA, SDT Q600, TA Instruments) were first performed on as-printed structures using a heating rate of 5 °C·min^{-1} up to 1000 °C under air conditions. Based on TGA-DTA results, the scaffolds were heat treated at 600 °C for 2 h, in air, using heating/cooling rates of 3 °C·min^{-1}. Afterwards, the 3D specimens were pressureless spark plasma sintered (SPS, SPS-510CE; Fuji Electronic Industrial Co., Ltd) in nitrogen atmosphere at temperatures ranging from 1650 to 1850 °C, with a holding time of 5 min at the maximum temperature. The heating rate was about 100 °C·min^{-1} up to 1600 °C and of 50 °C·min^{-1} from 1600 °C to the given set point.

The weight and dimensions of the sintered scaffolds were measured and the geometrical density (ρ_{geo}) was assessed. In addition, bulk density (ρ_{bulk}) -corresponding to the skeleton density - was determined by Archimedes' method as $\rho_{bulk} = P/(P_S - P_{DIW})$, where P, P_{DIW} and P_S are respectively the dry weight, the immersed weight (in de-ionized water), and the weight of the soaked scaffolds. Taking into account ρ_{geo} and ρ_{bulk} data, and the theoretical density of 3.30 g·cm^{-3} for the present AlN composition, the total porosity (π_{total}) and rod porosity (π_{rod}) were estimated, where π_{total} corresponded to the sum of the macro and microporosity of the entire scaffold (channels and skeleton). The

6

X-ray diffraction (XRD, Bruker D5000, Siemens) pattern of grinded and sintered 3D structures was employed to identify the crystalline phases after the SPS process. The ceramic scaffolds were observed by optical stereomicroscopy (Nikon SMZ1000) and field emission scanning electron microscopy (FESEM, Hitachi S-4700). The d_{50} values of the sintered materials were estimated by imaging analysis methods on FESEM images, considering more than 150 features. Characteristic parameters of the structures, i.e. the mean rod diameter (Ø), in-plane distance between two adjacent rods (a) and the distance between two equivalent layers in the z-direction (h), were measured on FESEM images (Fig. 1f).

S-S scaffolds were compression tested with their patterned sides facing compression platens, using a universal testing machine (ZwickiLine Z5.0 TS, Zwick-Roell) and a displacement rate of 0.5 mm·min^{-1}. Few of these samples were also subjected to loading/unloading cycles up to a maximum stress of 4 kN until completing a total of 100 cycles to estimate possible fatigue effects.

The thermal conductivity and the cooling rate studies were done on the 3D AlN to get a more complete representation of the thermal behavior of these structures. First, the effective thermal conductive (k_{eff}) of a single AlN rod was estimated from the Maxwell-Eucken's model [19]. Here, the rod was considered as a composite of two phases, one is the continuous ceramic phase and the other, comprises just the pores, which is valid for contents of the dispersed phase lower than 20 vol.%:

$$k_{eff} = k_t \frac{2k_t + k_{air} - 2(k_t - k_{air})\,\pi_{rod}}{2k_t + k_{air} + (k_t - k_{air})\,\pi_{rod}} \tag{1}$$

where k_t and k_{air} are the thermal conductivities of the AlN matrix and air (0.024 W·m^{-1}·K^{-1} at room temperature), respectively, and π_{rod} is the rod porosity (same as the skeleton). k_t was previously calculated by measuring the thermal diffusivity (α) of a

7

dense bulk sample from room temperature up to 800 ºC, in argon atmosphere, with a laser flash equipment (Thermaflash 2200, Holometrix Netzsch), and using the equation $k_t = \alpha \cdot \rho \cdot c_p$, where ρ is the sample density and c_p the specific heat [18]. To get realistic k data for present bulk AlN material, a dense disc (20 mm diameter and 3 mm thickness) was obtained from a burnt-out printed scaffold that was ground to achieve a powdered material representative of the scaffold. The resulting powers were sintered inside the SPS furnace at 1700 ºC for 5 min, in nitrogen atmosphere, and applying 50 MPa of uniaxial pressure.

The thermal conductivities in the longitudinal (k_L) and transverse (k_T) directions of the 3D structure were assessed through a simple model of thermal resistances that only depends on the cell parameters (Figure 1f) and k_{eff} of the rods as follows [20]:

$$k_L = \frac{\emptyset}{2a} k_{eff} \tag{2}$$

$$k_T = \frac{h \cdot \emptyset}{a^2} (1 - h/2\emptyset) \cdot k_{eff} \tag{3}$$

On the other hand, the thermal performing of the different patterned structures was analyzed by comparing their cooling rates. In this way, a micro-torch gas burner was focused during 30 s on the cell-side of the 3D AlN scaffolds and, then, the temperature of the structure was recorded for a period of 4 min that lasted the free cooling of the samples. The scaffolds were placed on an insulating fiber mat and the distance to the micro-torch was fixed to ~4 cm. A thermal imaging infrared camera (FLIR A325sc) registered the temperature profiles during the whole thermal cycle, and data presented in the next section correspond to the average value estimated into a square of about 6 x 6 mm^2 located at the center of the cell-side of the scaffold.

3. Results and discussion

The printable ink contained 70.2 wt.% of AlN, 20.6 wt.% of water (ultrapure plus water from the organics), and 9.2 wt.% of organics (5.8% H-PEI, 2.9% L-PEI, 0.1% MC, 0.4% PAA), that corresponded to 42.3, 40.4, and 17.3 in vol.%, respectively. The addition of H-PEI and L-PEI, acting as strong dispersants, allowed developing an ink composition with high AlN content, essential for keeping the robustness of the printed structures. Besides, the combination of those organics with MC (viscosifier) and PAA (flocculant) led to an ink with a shear thinning behavior, where the apparent viscosity diminished in more than four orders of magnitude as the shear rate augmented in the 10^{-1}-10^{2} s^{-1} interval (Figure 2a). Accordingly, AlN filaments were readily extruded through the nozzle tip, when the injector pressured on the barrel containing the ink, due to its low viscosity at high shear rates (Figure 2a). It is also remarkable that these pseudoplastic inks presented a high storage modulus (G'$\sim 10^{5}$ Pa), which is about one order of magnitude higher than the loss modulus (G''$\sim 10^{4}$ Pa) in the constant regime, and showed a cross over at the yield stress ($\tau_y \sim 180$ Pa), as Figure 2b depicts. The high G' and τ_y data predict a good shape retention of the printing filaments. In fact, the structures, independently of the CAD design, kept the filamentary shape and did not exhibit any deformation or damage during the building step, proving a high accuracy to the design architectures (Figure 2c).

DTA/TGA plots evidenced a weight loss of 16.4% up to 575 ºC (Figure 2d) for the as-printed AlN scaffolds, which matches the sum of the organics and water in the structure. Water and PAA evaporated and burnt-out, respectively, below 200 ºC; whereas both PEI, as well as MC, were eliminated in the 200-575 °C interval. At temperatures above 800 ºC, AlN started to oxidize and, hence, the burning-out temperature was fixed at 600 ºC to get a pure 3D AlN ceramic skeleton.
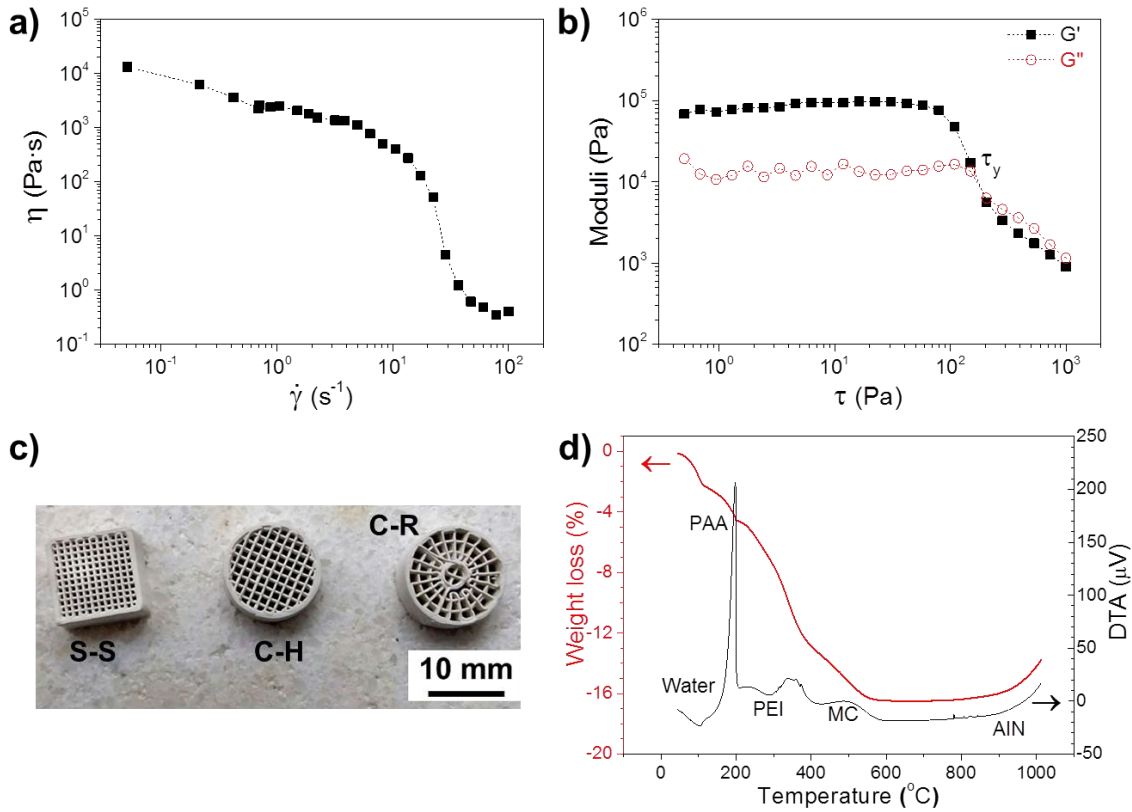
Figure 2. a) Apparent viscosity (η) versus shear rate ($\dot{\gamma}$) and b) shear storage (G') and loss (G'') moduli versus shear stress (τ) of the AlN inks. c) Some examples of as-printed square cuboid (S-S) and cylindrical (C-H and C-R) scaffolds. d) DTA/TGA (weight loss) of the as-printed AlN structures. DTA peaks associated to the removal of water, each organic, as well as to the AlN oxidation are identified.

A set of sintering tests was done on S-S scaffolds at temperatures ranging from 1650 to 1850 ºC. Densification in these structures progressively increased up to 1800 ºC, reaching ρ_{geo} and π_{total} values of 1.50 ± 0.07 g·cm^{-3} and 54.3 ± 2.0%, respectively (Figure 3a). Accordingly, the π_{rod} decreased from 40 to 14% for SPS treatments of 1650 and 1800 ºC, respectively (see Table S2 in the Supplementary Information). A further increase in the sintering temperature did not enhance the densification of the present structures and, therefore, 1800 ºC was selected as the most appropriate sintering temperature. The main crystalline phase in the S-S scaffolds sintered at 1800 ºC

10

corresponded to AlN (Figure 3b), although traces of secondary phases, in the form of

yttrium aluminates produced by the reaction between AlN and Y_2O_3 -in particular,

$Al_{12}Y_4O_9$ (YAM) and $Al_5Y_3O_{12}$ (YAG)- were also identified. The cross-section view of

the scaffold showed the perfectly straight filaments of the ceramic skeleton (Figure 3c),

with a d_{50}, estimated from FESEM images, of ~4.3 μm, indicating that a certain grain

growth took place during sintering since AlN raw powders had particle sizes in the

range of 0.8-2.0 μm.

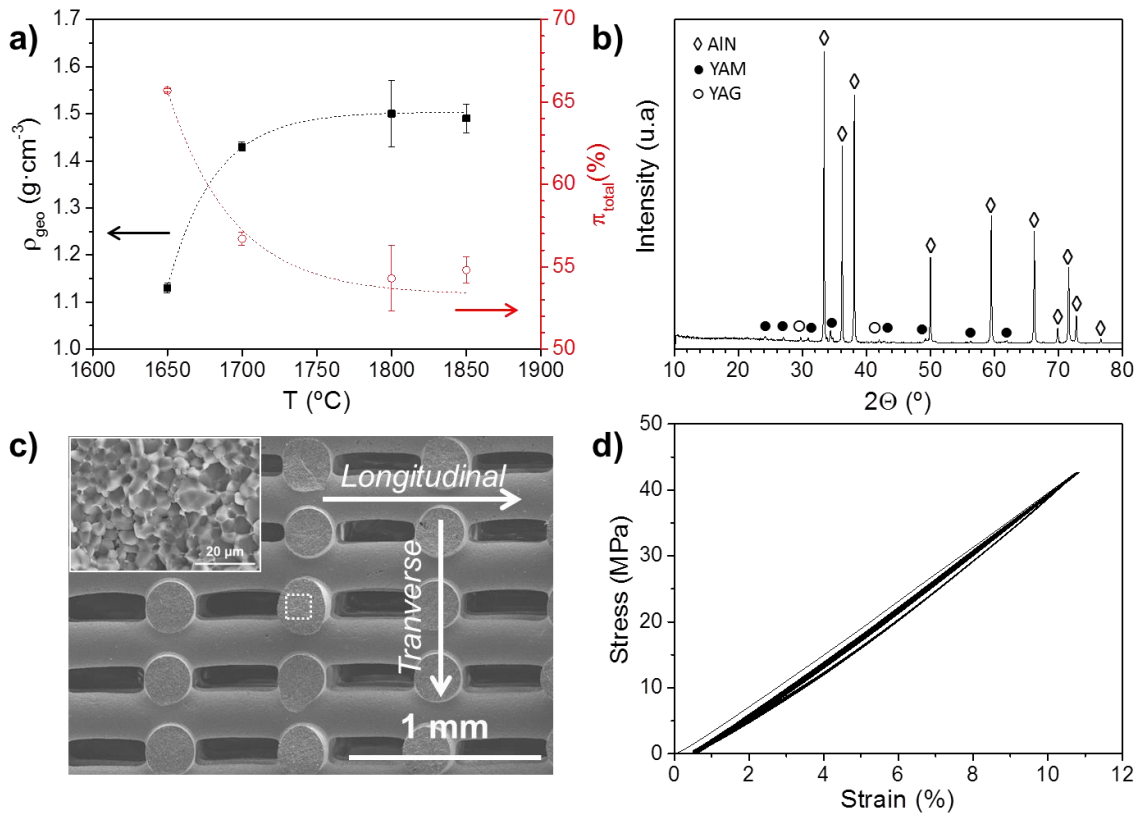Figure 3. a) Geometrical density (ρ_{geo}) and total porosity (π_{total}) of S-S scaffolds as a

function of the SPS temperature. b) XRD pattern, c) FESEM micrograph of the cross-

section view, and d) stress-strain recorded during 100 cycles for the S-S scaffold

sintered at 1800 °C. Arrows in c) indicate the longitudinal and transverse directions;

while the inset shows a high magnification FESEM image of the microstructure inside a

rod that corresponds to the area enclosed by a square.

11

The mechanical study on S-S scaffolds sintered at 1800 ℃ evidenced that the structures remained undamaged during the compression test up to the maximum load that permitted the load cell (5 kN), also showing a linear elastic behavior in the load-displacement plot for the whole load interval (Figure S1 in the Supplementary Information). Therefore, the compressive strength of these structures should be at least 53 MPa, which is placed among the highest values reported for 3D printed ceramics by Robocasting with similar π_{total} (~53%) [21]. Besides, stress-strain curves at a maximum load of 4 kN through 100 load-unload cycles (Figure 3d) illustrate that S-S scaffold recovered its original dimensions after each cycle, keeping its mechanical integrity and showing no evidence of fatigue.

The thermal diffusivity of the dense bulk material (see Figure S2 in the Supplementary Information) decreased with the temperature from 0.27 $cm^2 \cdot s^{-1}$ at 298 K to 0.08 $cm^2 \cdot s^{-1}$ at 1073 K. The thermal conductivity decreased with the temperature as well (Figure 4a), from a maximum value of 65 $W \cdot m^{-1} \cdot K^{-1}$ at room temperature down to 31 $W \cdot m^{-1} \cdot K^{-1}$ at 1073 K. These α and k_t data are about 25% lower than those attained for bulk dense specimens sintered with the same SPS conditions but employing the pristine ceramic powder composition (k_t ~87 $W \cdot m^{-1} \cdot K^{-1}$ at 298 K), instead of the crushed, milled and burnt-out robocast structures. This reduced k_t can probably be due to certain oxygen diffusion into the AlN lattice during the ink preparation, as some degree of AlN hydrolysis occurred. The oxygen atoms in solid solution would induce the formation of aluminum vacancies that further decrease the thermal conductivity through a phonon scattering mechanism [22]. In the case of the S-S scaffold sintered at 1800 ℃, the effective thermal conductive of the AlN rods (Figure 4a) was estimated from the equation (1), considering the k_t value of the bulk material, also included in Figure 4a,

12

and the porosity of the rods (14%), determined by the Archimedes' method. As a result, k_{eff} of the skeleton material decreased from 52 W·m⁻¹·K⁻¹ (at 298 K) to 25 W·m⁻¹·K⁻¹ (at 1073 K). Furthermore, k_{eff} of the 3D S-S structure in the longitudinal and transverse directions (Figure 4a) were assessed from equations (2) and (3) substituting k_{eff} of the rods and the cell parameters for the actual values ($\emptyset$ = 240 μm, h = 380 μm and a = 650 μm). In this way, k_L varied with temperature from 9.5 to 4.5 W·m⁻¹·K⁻¹, likewise, k_T decreased from 2.3 to 1.1 W·m⁻¹·K⁻¹ (Figure 4a). We would like to emphasize that these k_L and k_T values are close to the reported by Diaz-Moreno et al. (~5 W·m⁻¹·K⁻¹) [12], measured using the laser flash method, for AlN pellets of similar total porosity than the present 3D printed cellular structures (~60%). The thermal conductivity of the current structures in the longitudinal direction is ~ 310% higher than in the transverse one (Figure 4b). This difference can be explained by the fact that distinct variables affect the heat flow in each condition. In this way, k_L just depends on the number of rods oriented along the analyzed direction, that is, on the ratio between the diameter and the separation of the rods in the plane; while k_T depends on the number of available paths for heat flow in the z-direction and, following the design, it is strongly affected by the number of contacts and the effective contact area between adjacent orthogonal rods, i.e. the overlapping between adjacent layers. It should be noticed that this thermal anisotropy is equivalent to that observed for the electrical conductivity of analogous 3D printed SiC scaffolds that was also modeled using both analytical and finite element analysis [20].

Parallel calculations for estimating k_L and k_T (Figure 4b) were done for the square cuboid scaffolds sintered at 1800 ºC and for different rod separations as well (S-L, S-S and S-H). Data reflect the predicted dependence of the conductivity with the parameter a, decreasing as the rod separation augmented. Besides, k_L was always superior to k_T

13

and the thermal anisotropy increased with a, for example, k_L/k_T varied from ~3 for a = 0.47 mm (S-L) to ~6 for a = 1 mm (S-H).

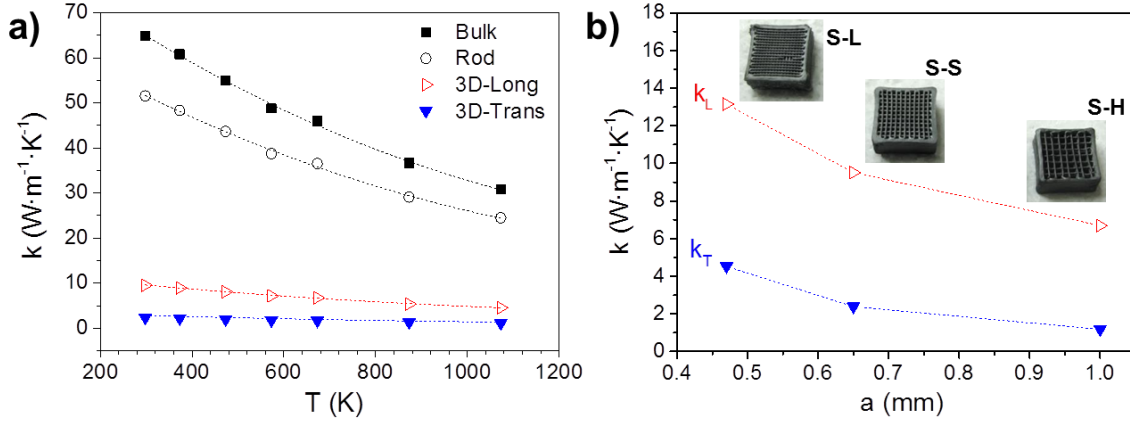Figure 4. a) Thermal conductivity (k) of bulk AlN samples as a function of the temperature. The effective thermal conductivity of the AlN rods, estimated from equation (1), and 3D S-S scaffolds sintered at 1800 ºC through the longitudinal (k_L) and transverse (k_T) directions are also plotted. b) k_L and k_T of square cuboids sintered at 1800 ºC as a function of the rod separation parameter, a. k_L and k_T data are calculated from equations (2) and (3).

If the effect of conduction along the framework is disregarded, cylindrical structures of similar pattern (C-H) would show the same thermal conductivity values than those estimated for cuboids (S-H) in both the longitudinal and transverse directions. In the case of cylindrical structures with a radial pattern (C-R) containing N radii, we can easily estimate the ratio between its axial thermal conductivity and that of similar cylindrical specimen with the standard pattern (C-H), as it would be given by the ratio between the corresponding number of contacts in each structure:

$$\frac{Contacts_{C-H}}{Contacts_{C-R}} = \frac{\left(\frac{2R}{a}\right)^2 \cdot \pi/4}{N\ of\ circles \cdot N\ of\ radii} \tag{4}$$

14

where R is the diameter (~5 mm in the present structures). The factor $\pi/4$ results from the volume ratio of a cylinder to a cuboid when the first is inscribed within the second (the diameter has the same length as the side of the cuboid). For current cylindrical scaffolds, the distance a is ~ 1 mm in the case of the orthogonal pattern; whereas the radial has 21 radii in the first layer and 3 circles in the second and, therefore, equation (4) gives a thermal conductivity for the radial design 0.8 times that of the standard pattern. According to equation (4), the thermal conductivity can be tuned by varying the number of inner circles or the number of radii. On the other hand, radially patterned structures should have isotropic in-plane thermal conductivity; while the standard cylindrical pattern would show certain radial anisotropy defined by the rod alignment along x and y directions. Thermal conductivity is a key parameter that can enhance the heat dissipation under stationary temperature gradients, and the present 3D printed structures stand out as a promising solution in applications where heat dissipation in a particular direction is required.

Figure 5a illustrates some examples of the heating and cooling curves recorded by the infrared camera on the cell-side surface of the 3D AlN S-S scaffolds for each sintering schedule. During the gas burner heating for 30 s, the temperature on the scaffold surface rose considerably (see inset in Figure 5a), until reaching a limit temperature (T_{max}) that depended on the sample sintering temperature (Figure 5a,b). When plotting T_{max} as a function of the total porosity of the specimens (Figure 5b), a clear correlation is not deduced. In this way, T_{max} ranged from ~1000 ºC for the for S-S structures sintered at 1800 ºC ($\pi_{total} = 52.9\%$) to ~1200 ºC for samples sintered at 1650 ºC ($\pi_{total} = 65.7\%$). However, this trend was not observed for the S-S scaffolds with different pattern designs sintered at 1800 ºC, all of them showing T_{max} ~1000 ºC despite their distinct total porosities (45-58%). It should be noticed that specimens sintered at 1800 ºC show

15

a dark gray color; whereas those sintered at lower temperatures display a lighter color (see images of the scaffolds in Figure 5b). Therefore, the radiation effect is expected to be higher in the darkest scaffolds affecting the balance between absorbing and emitting heat and, therefore, T_{max} decreased. On the other hand, cylindrical periodic lattices sintered at 1800 ºC, also dark grey colored, showed higher T_{max} values (1150 and 1075 ºC for C-H and C-R, respectively) than the alike S-S scaffold (Figure 5b), although their masses are significantly lower (0.47 and 0.53 g, respectively) than that of S-S structures (0.73 g).

As seen in Figure 5c, the experimental data of the cooling rate showed a clear deviation from the straight line plot linked to the simple exponential cooling curve of Newton's law. That deviation occurred during the first ~20-40 s, depending on the sintering temperature, that corresponded to temperature differences ranging from 350 ºC ,in the case of the specimen sintered at 1800 ºC, up to 650 ºC, for the specimen sintered at 1650 ºC. Since the range of validity of Newton's law does just depend on the ratio of convective to radiative heat transfer [23], this result agrees with the lower emissivity of 1650 ºC specimens for which the radiative dissipation exhibited a lower impact.

In order to support that the heat transfer from the scaffold to the surrounding air due to the convection and radiation can be analyzed using the Newton's law, it is assumed that the internal heat flow is much faster than the heat loss from the surface (i.e. Biot number, Bi, << 1), and, hence, there is a temperature equilibrium within the specimen. In this way, Bi can be estimated considering typical values for heat-transfer coefficients for free convection (solids to gases) in the range of 2-25 $W·m^{-2}·K^{-1}$, [23] and the values of the thermal conductivity deduced for the 3D structures (maximum $k_L = 13$ $W·m^{-1}·K^{-1}$ and minimum $k_T = 1$ $W·m^{-1}·K^{-1}$, taken from Figure 4b). As result, Bi values in the range of 2.5 x 10^{-1} - 1.5 x 10^{-3} are obtained for a 10 mm scaffold size.

16

Accordingly, in the present case, the cooling profiles for the scaffolds can be perfectly fitted ($R^2 > 0.999$) to the following second order exponential function:

$$T\left(t\right) = y_0 + A_1 e^{-t/\tau_1} + A_2 e^{-t/\tau_2} \tag{5}$$

where y_0 corresponds to the environment temperature and A1 and A2 parameters are related to the difference between the starting and the final temperatures. The resulting fitting parameters for all the structures, using the corresponding T_{max} as starting points, are collected in Table S1 of the Supplementary Information.

It can be inferred from Figure 5d that radiation cooling was predominant in S-S structures sintered at 1800 °C ($A_1/A_2 = 0.50$), particularly when compared to ratios of samples sintered at 1650 °C (0.28) and 1700 °C (0.35). Furthermore, the A_1/A_2 ratio was quite similar (0.5-0.6) for the S type scaffolds, independently of the rod separation; while for cylindrical periodic lattices, the ratio was slightly higher (~0.68), fact that could be related to a lower contribution of convection cooling. The higher A_1/A_2 values for specimens sintered at 1800 °C can be explained by their higher emissivity, proving again that, despite convection is the main mechanism for heat transfer in the present 3D highly porous structures and under the current experimental conditions, radiative heat transfer plays a significant role at the onset of cooling for temperatures above 500 °C.
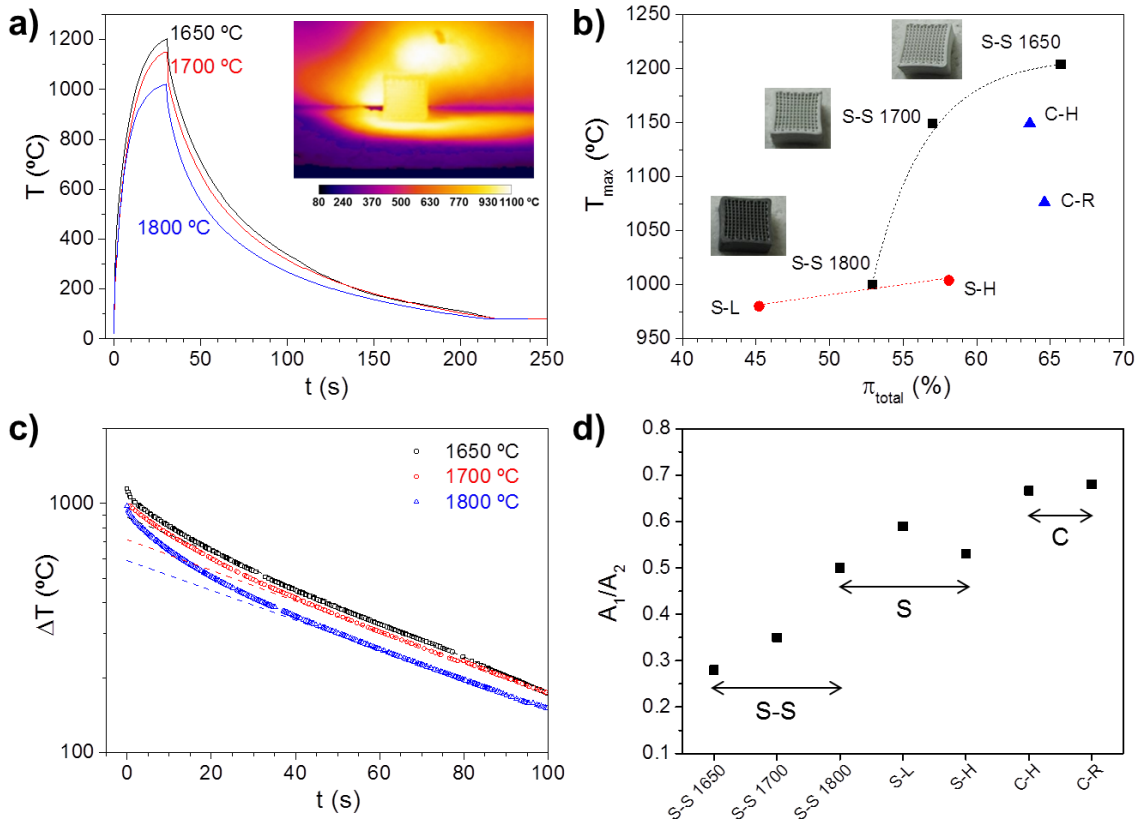
17

Figure 5. a) Experimental heating and cooling curves recorded for 3D S-S scaffolds sintered at distinct SPS temperatures (1650-1800 °C). The inset shows an example (S-S at 1800 °C) of the thermographic image at the maximum temperature (T_{max}) after 30 s of the heating process. b) T_{max} as a function of the total porosity (π_{total}) for all patterned structures. Images of S-S scaffolds are also included to illustrate their distinct darkness. c) Experimental data of the cooling rate (empty symbols) for 3D S-S scaffolds sintered at different temperatures and linear fitting (dashed line) according to the Newton's law. d) A_1/A_2 ratio for the different scaffolds as a function of the sintering temperature (S-S specimens) and the patterned design (cuboid -S- and cylindrical -C-).

Regarding the time constants data (τ_1 and τ_2, see Table S1 in the supplementary information), both related to the heat transfer rate, no significant changes were detected with the sintering temperature but with the patterned design.

18

As the time constant is given by:

$$\tau = \frac{\rho c V}{h' A} \tag{6}$$

where ρ is the density, c the specific heat, V the volume, h' the total heat transfer exchange coefficient, and A the exchange surface area of block, τ_1 and τ_2 data plotted as a function of $\frac{\rho V}{A}$ (Figure 6a) show the expected increasing trend, with slopes of 5.2 x 10^{-3} and 24.0 x 10^{-3} $m^2 \cdot s \cdot g^{-1}$ for τ_1 and τ_2, respectively, which gives h' values of 142 $W \cdot m^{-2} \cdot K^{-1}$ for τ_1 and 30 $W \cdot m^{-2} \cdot K^{-1}$ for τ_2, considering $c = 727$ $J \cdot K^{-1} \cdot kg^{-1}$. This τ_2 value is close to the typical one (20-25 $W \cdot m^{-2} \cdot K^{-1}$) for heat-transfer coefficients for free convection (small object). On the other hand, the radiation heat transfer would increase with $\sim T^3$ and for high ΔT (> 400 ºC), h' is estimated to be $\sim$100-200 $W \cdot m^{-2} \cdot K^{-1}$, which is in good agreement with the deduced value from the τ_1 data fitting.

Considering that the structure density and the macroporosity (π_{macro}) depend on the scaffold parameters (h, a, ϕ) as:

$$\rho = \rho_{rod} \left(\frac{\pi \cdot \text{Ø}^2}{2 \cdot a \cdot h} + \frac{V_{ext}}{V_{total}} \right) \tag{7}$$

$$\pi_{macro} = 100 \cdot \left(1 - \frac{\pi \cdot \text{Ø}^2}{2 \cdot a \cdot h} - \frac{V_{ext}}{V_{total}} \right) \tag{8}$$

which is geometrically deduced by accounting the solid volume of the rods [19], the volume of the external framework (V_{ext}), and the total volume of the specimen (V_{total}), the scaffold thermal performance could be tuned by varying h, a, ϕ in a controlled way.

When representing τ_1 and τ_2 data versus π_{macro} (see Table S2 in the Supplementary Information) for all structures (Figure 6b), a certain inverse linear dependence was observed, with both time constants decreasing as porosity augmented, in agreement with

19

previous studies that demonstrated how macroporosity favors heat transfer [24,25].

Better linear fitting was achieved when time constants were represented vs. rod

separation (Figure 6c), showing that the heat dissipation, both radiative and convective,

increased with the parameter *a,* also linked to the scaffold porosity. Ferrari et al. [24]

reported a similar effect by 3D thermo-fluid dynamics simulations in a cubical lattice as

a function of the rod diameter. These authors observed that the heat transfer coefficient

increased as Ø decreased, or the rod separation augmented. Accordingly, the above

described relationship between time constants and key geometrical parameters of the 3D

structures may be meaningful employed to select the type of design initially more

appropriate to achieve a fixed cooling profile, thus reducing the variables to optimize in
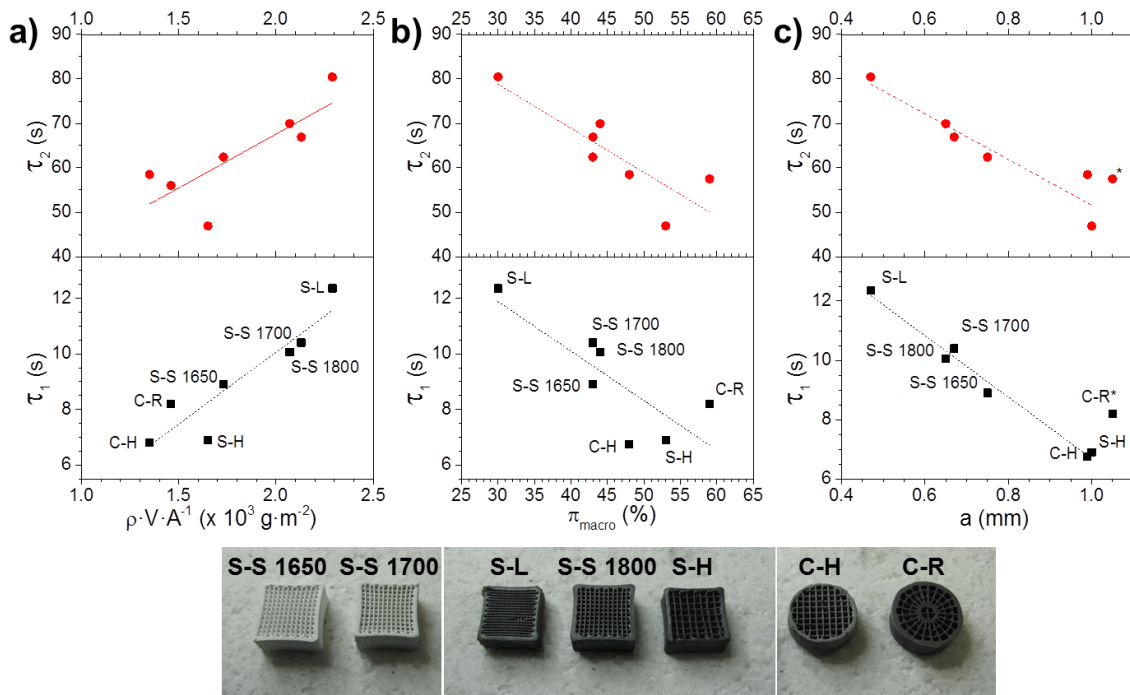
the printing process.

Figure 6. Time constants τ_1 and τ_2 of all patterned scaffolds as a function of: a) $\frac{\rho V}{A}$, b)

macro porosity (π_{macro}), and c) rod separation parameter, *a*. At the bottom of the panel,

20

optical images of the scaffolds are shown. *a* parameter for C-R structures in c) corresponds to an average value between the inner and outer arcs.

4. Conclusions

3D cellular AlN architectures with different pattern designs have been successfully manufactured by robocasting. The printed structures after pressureless spark plasma sintering are extraordinarily robust, with compressive strengths above 53 MPa, and capable of supporting up to 100 loading/unloading cycles without damage. The pattern geometry actually controls the thermal performance of the scaffolds, in particular, their effective thermal conductivity and heat dissipation functional forms. Orthogonal patterned structures are thermally anisotropic, with predicted thermal conductivity in the longitudinal direction up to six times higher than in the transverse one, decreasing the conductivity in both directions as the rod separation augments. Heat dissipation during free cooling tests is governed in all the structures by convection and radiation processes, the latter especially dominating at the onset of cooling until reaching temperatures ~500 ºC. Furthermore, heat dissipation intensifies as the macroporosity and rod separation increase, or the solid area of the structures diminishes. Either cuboid or cylindrical orthogonal lattices with large rod spacing are best suited for heat dissipation matters, although, in contrast, the thermal conduction is reduced. In summary, 3D printing arises as a promising technology to tailor the thermal performance of cellular materials through the control of their patterned structures.

21

References

[1] G.A. Slack, Nonmetallic crystals with high thermal conductivity, J. Phys. Chem. Solids 34 (1973) 321-335, https://doi.org/10.1016/0022-3697(73)90092-9

[2] S. Kume, M. Yasuoka, S.K. Lee, Dielectric and thermal properties of AlN ceramics, J. Eur. Ceram. Soc. 27 (2007) 2967-2971, https://doi.org/10.1016/j.jeurceramsoc.2006.11.023

[3] J.H. Harris, Sintered aluminum nitride ceramics for high-power electronic applications, JOM 50 (1998) 56-60, https://doi.org/10.1007/s11837-998-0130-z

[4] J. Broughton, V. Smet, R. R. Tummala, Y. K. Joshi, Review of thermal packaging technologies for automotive power electronics for traction purposes, J. Electron. Packag. 140 (2018) 040801, https://doi.org/10.1115/1.4040828

[5] X. Guo, Q. Xun, Z. Li, S. Du, Silicon carbide converters and MEMS devices for high-temperature power electronics: a critical review, Micromachines 10 (2019) 406, https://doi.org/10.3390/mi10060406

[6] M. Ding, Y. Shi, J. Xie, D. Zhou, Y. Wang, F. Lei, L. Zhang, Optimization of non-aqueous tape casting of high solid loading slurry for aluminum nitride ceramic substrates, Int. J. Appl. Ceram. Technol. 17 (2020) 285-295, https://doi.org/10.1111/ijac.13344

[7] J. Xue, M. Dong, J. Li, G. Zhou, S. Wang, Gelcasting of aluminum nitride ceramics, J. Am. Ceram. Soc. 93 (2010) 928-930, https://doi.org/10.1111/j.1551-2916.2009.03489.x

[8] L. Guo, J. Yang, Y. Feng, T. Qiu, Non-aqueous gelcasting of AlN ceramics using a low-toxicity monomer (DMAA) as gelling agent, Ceram. Inter. 44 (2018) 1621-1626, https://doi.org/10.1016/j.ceramint.2017.10.083

[9] H. Lu, M. Qin, H. Wu, Q. He, C. Liu, X. Mu, Y. Wang, B. Jia, X. Qu, Effect of AlN powders on the debinding and sintering behavior, and thermal conductivity of injection molded AlN ceramics, Ceram. Inter. 45 (2019) 23890-23894, https://doi.org/10.1016/j.ceramint.2019.08.183

[10] D. Huang, Z. Liu, J. Harris, X. Diao, G. Liu, High thermal conductive AlN substrate for heat dissipation in high-power LEDs, Ceram. Int. 45 (2019) 1412-1415. https://doi.org/10.1016/j.ceramint.2018.09.171

[11] N. R. Jankowski, L. Everhart, B. R. Geil, C. W. Tipton, J. Chaney, T. Heil, W. Zimbeck, Stereolithographically fabricated aluminum nitride microchannel substrates for integrated power electronics cooling, in 11th Intersociety Conference on Thermal and Thermomechanical Phenomena in Electronic Systems, Orlando, FL, 2008, pp. 180-188, https://doi.org/10.1109/itherm.2008.4544269

[12] C. A. Díaz-Moreno, Y. Lina, A. Hurtado-Macías, D. Espalin, C. A. Terrazas, L. E. Murr, R. B. Wicker, Binder jetting additive manufacturing of aluminum nitride components, Ceram. Inter. 45 (2019) 13620-13627, https://doi.org/10.1016/j.ceramint.2019.03.187

[13] Z. Huang, X. Wang, J. Yang, C. Yao, S. Li, L. Zheng, Z. Wu, C. Lyu, Aluminum nitride ceramic material for 3D printing and preparation method thereof , Chinese Patent, Application number CN20161160210 20161128.

[14] W. Duan, S. Li, G. Wang, R. Dou, L. Wang, Y. Zhang, H. Li, H. Tan, Thermal conductivities and mechanical properties of AlN ceramics fabricated by three dimensional printing, J. Eur. Ceram. Soc. 40 (2020) 3535-3540, https://doi.org/10.1016/j.jeurceramsoc.2020.04.004

[15] J. A. Lewis, Direct ink writing of 3D functional materials, Adv. Funct. Mater. 16 (2006) 2193-2204, https://doi.org/10.1002/adfm.200600434

[16] E. Peng, D. Zhang, J. Ding, Ceramic robocasting: recent achievements, potential, and future developments, Adv. Mater. 30 (2018) 1802404, https://doi.org/10.1002/adma.201802404

[17] Y.-L. He, H.-W. Wu, Investigation on low-temperature sintered AlN nanoceramics with high thermal conductivity, Int. J. Appl. Ceram. Technol. 16 (2019) 2101-2106, https://doi.org/10.1111/ijac.13208

[18] I. N. G. Simsek, A. Nistal, E. Garcia, D. Pérez-Coll, P. Miranzo, M. I. Osendi, The effect of graphene nanoplatelets on the thermal and electrical properties of aluminum nitride ceramics, J. Eur. Ceram. Soc. 37 (2017) 3721-3729, https://doi.org/10.1016/j.jeurceramsoc.2016.12.044

[19] A. Eucken, Fortchg. Gebiete Ingenieurw. B3 Forschungsheft. 1932,16, 353.

[20] B. Román-Manso, F. M. Figueiredo, B. Achiaga, R. Barea, D. Pérez-Coll, A. Morelos-Gómez, M. Terrones, M. I. Osendi, M. Belmonte, P. Miranzo, Electrically

functional 3D-architectured graphene/SiC composites, Carbon 100 (2016) 318-328,

https://doi.org/10.1016/j.carbon.2015.12.103

[21] M. Belmonte, M. Koller, J. J. Moyano, H. Seiner, P. Miranzo, M. I. Osendi, J.

González-Julián, Multifunctional 3D-printed cellular MAX-phase architectures, Adv.

Mater. Technol. 4 (2019) 1900375, https://doi.org/10.1002/admt.201900375

[22] L. Qiao, H. Zhou, H. Xue, S. Wang, Effect of Y_2O_3 on low temperature sintering

and thermal conductivity of AlN ceramics, J. Eur. Ceram. Soc. 23 (2003) 61-67,

https://doi.org/10.1016/S0955-2219(02)00079-1

[23] M. Vollmer, Newton's law of cooling revisited, Eur. J. Phys. 30 (2009) 1063-1084,

https://doi.org/10.1088/0143-0807/30/5/014

[24] L. Ferrari, M.C. Barbato, A. Ortona, C. D'Angelo, Convective heat transfer in

cellular ceramic: A 3D numerical solution, in: P.J. Meyer (Ed.), In 10th International

Conference on Heat Transfer, Fluid Mechanics and Thermodynamics, HEFAT, 2014,

http://hdl.handle.net/2263/44474

[25] M. Pelanconi, M. Barbato, S. Zavattoni, G.L. Vignoles, A. Ortona, Thermal design,

optimization and additive manufacturing of ceramic regular structures to maximize the

radiative heat transfer, Mater. Design 163 (2019) 107539,

https://doi.org/10.1016/j.matdes.2018.107539

25

Supplementary Information

*Declaration of Interest Statement

Declaration of interests

☒ The authors declare that they have no known competing financial interests or personal relationships that could have appeared to influence the work reported in this paper.

☐ The authors declare the following financial interests/personal relationships which may be considered as potential competing interests: